Synthesis of Ag@AgI plasmonic photocatalyst with enhanced visible-light photocatalytic activity

Xiaoyang Yue[a], Lirong Kong[a,b], Xiang Xu[a], Xiaoping Shen[a,*], Xuli Miao[a], Zhenyuan Ji[a], Jun Zhu[a]

[a]School of Chemistry and Chemical Engineering, Jiangsu University, Zhenjiang 212013, China, email: xiaopingshen@163.com (X. Shen)
[b]School of Material Science and Engineering, Jiangsu University, Zhenjiang 212013, China

ABSTRACT

The plasmonic photocatalyst Ag@AgI with narrow size distribution was synthesized by a precipitation reaction between Ag^+ ions and I^- ions in ethylene glycol with the assistance of polyvinylpyrrolidone K30, followed by reducing the Ag^+ ions on the surface of AgI particles to Ag^0 through a light-induced chemical reduction process. The obtained Ag@AgI photocatalyst shows strong absorption in the visible-light region, and also exhibits enhanced photocatalytic activity and stability toward the degradation of organic contaminant under visible-light irradiation. The possible degradation pathways of Rhodamine B were also discussed in detail. The excellent photocatalytic performance makes the Ag@AgI composite a promising photocatalyst for organic pollutant treatment.

Keywords: Silver iodide; Silver; Plasmonic; Photocatalysis; Degradation mechanism

1. Introduction

Photocatalysis has potential applications in the control and treatment of environmental pollutants. However, most of the widely investigated photocatalysts could only exhibit low utilization efficiencies for visible light, which greatly limit their practical application [1,2]. For example, TiO_2 has been regarded as one of the most popular photocatalysts due to its chemical stability, photostability, low cost, nontoxicity, and abundance in nature [3–7]. However, since the band gap of TiO_2 is greater than 3.0 eV, it is only photocatalytically active under UV light irradiation, which only accounts for about 4% of the solar energy [8]. In addition, the quick recombination rate of photo-generated electron–hole pairs in TiO_2 results in its low quantum efficiency, which also limits its photocatalytic performance [9]. In order to solve these problems, plenty of efforts have been paid on the preparation of visible-light-driven catalysts, and simultaneously improving their photocatalytic activities by doping them with heteroatoms [10–14], composing them with photosensitizers [15,16], and constructing them with suitable semiconductors to form heterostructures [17,18]. However, due to the limited catalytic activity and stability of semiconductors, these catalysts still could not meet the requirements for practical application in commercial use. As a result, searching for photocatalyst with high visible-light utilization efficiency is still a challenge.

In recent years, "plasmonic photocatalyst" has attracted worldwide attention [19]. Since the noble metal (Ag, Au, and Pt) nanoparticles could exhibit excellent absorption in the visible-light region due to the surface plasmon resonance effect, when they are attached to the surface of the semiconductor, the absorption of visible light by the noble metal-semiconductor composite could be greatly improved [20–30]. Chen et al. [22] reported the preparation of Au/ZrO_2 and Au/SiO_2 photocatalysts, and the photocatalytic activities of the obtained products under visible-light are greatly improved by the surface plasmonic effect of the gold nanoparticles. Xiang et al. [23] successfully prepared the Ag/TiO_2 plasmonic photocatalyst with greatly improved photocatalytic efficiency toward the degradation of RhB under visible-light irradiation.

* Corresponding author.

Due to the smaller band gap as well as the higher visible-light absorption of silver halides (AgX, X = I, Br, Cl), they have been widely investigated as host for photosensitive materials [31–33]. Among the noble metal/AgX composite photocatalyst, Ag@AgX composite photocatalysts are of particular interest due to their high stability and the good contact between Ag and AgX [33–39]. In detail, AgX can be partially in situ converted into Ag nanoparticles, thus the effective interfacial charge transfer formed between them and the significantly enhanced photocatalytic activities [27,28,34,35,37]. In this work, we propose a simple and rapid method for the preparation of highly stable Ag@AgI plasma photocatalyst with narrow size distribution. First, AgI nanoparticles are formed by the precipitation of silver nitrate and sodium iodide in the presence of surfactant polyvinylpyrrolidone (PVP), and then the AgI sample is treated under visible-light irradiation to generate metal Ag on AgI surface. By adjusting the concentration of PVP in the reaction system, the morphology and size of Ag@AgI can be well controlled. The photocatalytic activity of the obtained product is evaluated through the photodegradation of Rhodamine B (RhB) under visible light, and the degradation mechanism for RhB is discussed in detail.

2. Experimental

2.1. Materials

Silver nitrate, sodium iodide, ethylene glycol, RhB, polyvinylpyrrolidone K30, and ethanol were purchased from Shanghai Chemical Reagent Co. Ltd. (China). All chemicals used in this study were of analytical grade and used without further purification. Meanwhile, the deionized water was used in all the experiments.

2.2. Preparation of Ag@AgI photocatalysts

For the preparation of Ag@AgI catalysts, 15 mL of ethylene glycol was first cooled to 0°C in an ice bath, and then 2 mmol of $AgNO_3$ and 3 mmol of the surfactant PVP were dissolved in the above solvent to form a clear solution. Meanwhile, 2 mmol of NaI was added to another 15 mL of ethylene glycol, forming a homogeneous solution by sonication at room temperature, which was then slowly added to the above $AgNO_3$/PVP solution followed by vigorous stirring for 30 min. The products were obtained by centrifugation, and washed with absolute ethanol for several times before being dried at 45°C in vacuum for 12 h. The obtained AgI sample was dispersed in water and irradiated with a 250 W Xe lamp with a 420 nm cutoff filter for ca. 10 min to prepare Ag@AgI plasmonic photocatalyst. This product was labeled as PVP-3. For comparison, with other experimental conditions unchanged, the amount of PVP was adjusted to 0, 0.5, 1, and 5 mmol, respectively, and the prepared samples were correspondingly denoted as PVP-0, PVP-0.5, PVP-1, and PVP-5.

2.3. Characterization

Scanning electron microscopy measurements were performed on a JSM-6480 microscope equipped with energy dispersive X-ray (EDX) spectrometry. Transmission electron microscopy (TEM) experiments were performed on a JEM-2100 electron microscope with an acceleration voltage of 200 kV. The phases of the as-obtained products were characterized by X-ray diffraction (XRD) on a Bruker D8 Advance diffractometer with Cu Ka radiation at a scanning rate of 7° min⁻¹. Ultraviolet–visible (UV–vis) absorption spectra were recorded with a UV-1800PC UV–vis spectrophotometer and UV–vis diffuse reflectance spectra were conducted with a UV-2450 UV–vis spectrophotometer. The X-ray photoelectron spectroscopy (XPS) measurements were performed on a Thermo ESCALAB 250XI spectrometer. The electron spin resonance (ESR) signals of radicals spin-trapped by spin-trap reagent 5,5-dimethyl-1-pyrroline N-oxide (DMPO) were examined on a Bruker EPR A300-10/12 spectrometer.

2.4. Photocatalytic performance measurement

The photodegradation reaction was conducted in a GHX-3 photochemical reactor (Science and Education Equipment Co., Ltd, Yangzhou, China). In this work, the photocatalytic activities of Ag@AgI were evaluated by the photocatalytic degradation of RhB under visible-light irradiation. A 250 W Xe lamp with a 420 nm cutoff filter was used as the visible-light source, which was positioned at ca. 10 cm away from the photocatalytic reactor with a light intensity of ca. 256 mW cm⁻² (measured by FZ-A radiometer) during the photocatalytic process. A water layer is placed between the light reaction system and the light source to remove the thermal effect generated by the Xe lamp. The photocatalytic experiments were carried out at room temperature as follows: 0.1 g of Ag@AgI catalysts was added to 100 mL of RhB solution with a concentration of 10 mg L⁻¹. Before illumination, the suspension was stirred in the dark for 1 h to ensure the establishment of an adsorption–desorption equilibrium between the photocatalyst and RhB. Then, the obtained dispersion was irradiated by visible-light under stirring. At regular intervals, 4 mL of the suspension was pipetted into a centrifuge tube and centrifuged at 8,000 rpm for 2 min to separate the residual photocatalysts from the RhB solution. The absorbance of the supernatant at 553 nm was detected by UV-2450 spectrophotometer to monitor the concentration of RhB. The photodegradation ratio was calculated using the relative concentration (C/C_0) of the RhB, where C_0 is the calculated concentration of RhB after adsorption equilibrium, and C is the residual concentration at different irradiation time. In the recycle experiments, after each cycle, Ag@AgI photocatalysts were separated from the solution by centrifugation, washed with ethanol and deionized water, respectively, and then redispersed in the dye solution for next cycle.

2.5. Determination methods for the degradation products

The final products were determined by a gas chromatography interfaced a HED-EM mass spectrometer (GC/MS, Agilent 7890A/5975C, USA). The degraded solution was pretreated as follows: it was first centrifuged to remove the residual catalysts, and then the pH of the supernatant was adjusted to 2.0 by 10 wt% HCl solution. 30 mL of the supernatant solution was extracted with 30 mL of dichloromethane for three times. The obtained solution was dehydrated by using anhydrous sodium sulfate and finally concentrated to 1 mL. After that, 0.5 mL of *bis*(trimethylsilyl) trifluoroacetamide was added into the above solution at 50°C and treated for 30 min to silanize the obtained product. 1.0 μL

of the above silanized sample was tested by the GC/MS equipped with DB-5MS column (fused-silica capillary column, 30 × 0.25 mm i.d., 0.25 μm film thickness with a 5% equivalent polysilphenylene siloxane) under splitless mode. The programmed temperature was set to 60°C for 1 min and then raised from 60°C to 260°C at a rate of 10°C min^{-1}.

2.6. Photoelectrochemical measurements

Electrochemical measurements were performed on a 760D electrochemical analyzer (ChenHua Instruments, Shanghai, China) using a standard three-electrode system. The platinum wire and saturated calomel electrode were used as counter electrodes and reference electrodes, respectively. 0.1 M Na$_2$SO$_4$ aqueous solution was used as the electrolyte. The working electrode was a F-doped tin dioxide (FTO) glass deposited with the as-prepared sample with a light irradiation area of 1.0 cm^2. In detail, the working electrode was prepared as follows: First, 4 mg of the as-prepared samples were dispersed in a mixed solution of 980 μL of ethanol and 20 μL of Nafion by sonication to form a homogeneous suspension, afterwards 0.1 mL of the above suspension was coated on an FTO glass plate and dried overnight at 45°C to ensure that the samples were tightly attached on the FTO. A 300 W Xe lamp was utilized as the light source, and the distance between the illumination light source and the photocathode was fixed at 25 cm.

3. Results and discussion

3.1. Characterization of the photocatalysts

Ag$^+$ cations and I$^-$ anions were precipitated in ethylene glycol solution to form AgI nanoparticles with the assistance of polymeric surfactant PVP. At lower temperatures, ethylene glycol exhibits a high viscosity, which could inhibit the diffusion of Ag$^+$ and I$^-$ ions. As a result, the AgI was generated at a very fast nucleation rate and a relatively slower growth rate, which is beneficial to form small and uniform AgI nanoparticles. More importantly, the PVP, which was adsorbed on the surface of AgI nanoparticles as a protecting agent, also restricted the quick growth of AgI nanoparticles and favored the formation of uniform nanoparticles.

The phase structures of the as-prepared Ag@AgI photocatalysts were characterized by the XRD. The XRD pattern of PVP-3 is shown in Fig. 1(a), in which the peaks at 2θ = 22.30°, 23.62°, 25.25°, 39.20°, 42.56°, and 46.28° can be well indexed to the (100), (002), (101), (110), (103), and (112) crystal planes of AgI (JCPDS card no. 09-0374) [40].

The diffraction peaks from Ag metal are not obvious in the XRD pattern, which can be ascribed to the low content of Ag in the as-prepared sample. EDX spectrum was also used to confirm the chemical composition of PVP-3. As shown in Fig. 1(b), the sample consists of Ag and I elements and the molar ratio of Ag to AgI is approximately 1:16, proving that the product is composed of AgI and Ag.

TEM was used to characterize the morphology and size of the as-prepared samples. It was found that the PVP amount in the reaction system had an important influence on the final morphology and size of the formed Ag@AgI nanocrystals. The Ag@AgI nanocrystals with different shapes and sizes can be obtained by adjusting the PVP content. The corresponding TEM images of PVP-0, PVP-0.5, PVP-1, PVP-3, and PVP-5 are shown in Fig. 2. PVP-0 synthesized without PVP exhibits irregular shapes and big particle size (Figs. 2(a) and (b)). Due to the shortage of PVP protecting, the particles show severe agglomeration. When 0.5 mmol of PVP was used, the product of PVP-0.5 exhibits an improvement in the homogeneousness of size and shape with an average diameter of about 39.5 nm (Fig. 2(c)). Along with the increment of the PVP amount, the PVP-1 and PVP-5 consist of well-dispersed nanoparticles with an average diameter of about 30.6 and 30.2 nm, respectively (Figs. 2(d) and (f)). As shown in
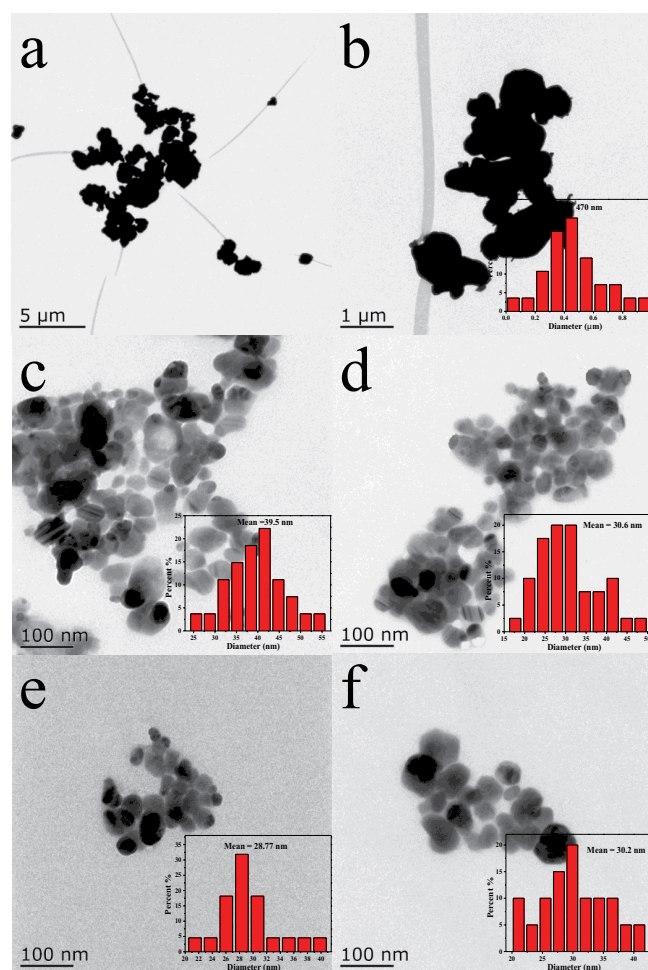
Fig. 2. TEM images of the as-prepared Ag@AgI samples obtained with different PVP amounts: (a and b) PVP-0, (c) PVP-0.5, (d) PVP-1, (e) PVP-3, and (f) PVP-5.

Fig. 1. (a) XRD pattern and (b) EDX spectrum of the as-prepared sample of PVP-3.

Fig. 2(e), PVP-3 is composed of a large number of nanocrystals, and the nanocrystals are well-dispersed and exhibit a uniform size distribution with an average size of about 28.8 nm (inset in Fig. 2(e)). According to the above results, it can be concluded that increasing the amount of PVP in a certain range favors the formation of small and uniform Ag@AgI particles, but when beyond the optimal amount (3 mmol), the further addition of PVP has little effect on the morphology and size of the Ag@AgI nanocrystals. Regrettably, the high-resolution TEM images could not be obtained due to the decomposition of AgI nanocrystals under high-energy electron beam irradiation.

XPS measurement was further performed to comprehend the surface composition and chemical states of the Ag@AgI samples. From the XPS survey spectrum in Fig. 3(a), the elements of Ag and I were detected in Ag@AgI, which is in good consistent with the composition of the composite (C1s peak can be ascribed to the adventitious hydrocarbon from XPS instrument itself). As shown in Fig. 3(b), the peaks of Ag $3d_{3/2}$ and Ag $3d_{5/2}$ appeared at 374.1 and 368.1 eV, which belonged to Ag^+ in AgI phase. And no Ag^0 was found. However, after the visible-light irradiation, as shown in Fig. 3(c), each peak of the Ag element can be deconvoluted into two peaks.

The Ag $3d_{3/2}$ peak was resolved into 374.0 and 374.4 eV, and the Ag $3d_{5/2}$ peak into 368.0 and 368.3 eV. Both the peaks at 374.0 and 368.0 eV corresponded to the Ag^+ in AgI phase. The other two peaks at 374.4 and 368.3 eV resulted from the metallic Ag^0 [41,42]. The XPS results for silver confirmed that metal Ag was in situ grown on AgI via visible-light irradiation. The XPS spectra of I 3d are shown in Fig. 3(d). The spectra of I 3d shows doublet peaks at 619.1 (I $3d_{5/2}$) and 630.6 eV (I $3d_{3/2}$), which are assigned to I^- in AgI and there were no peaks above 620.0 eV for I $3d_{5/2}$, indicating that I_2 did not exist in the as-prepared composite [43].

As mentioned earlier, noble metal particles play an important role in the light absorption of the as-prepared composite photocatalysts. Fig. 4 shows the UV-vis diffuse reflectance spectra of Ag@AgI nanoparticles and the pure AgI nanoparticles, from which it is found that the Ag@AgI plasmonic photocatalyst has a stronger absorption in the visible-light regions, which is in good agreement with the previous report [44]. The absorption at 200–450 nm derives from the characteristic absorption of AgI, and the absorption at 450–800 nm can be attributed to the surface plasmon resonance effect of Ag nanoparticles. The enhanced visible-light absorption of Ag@AgI composites is beneficial to the
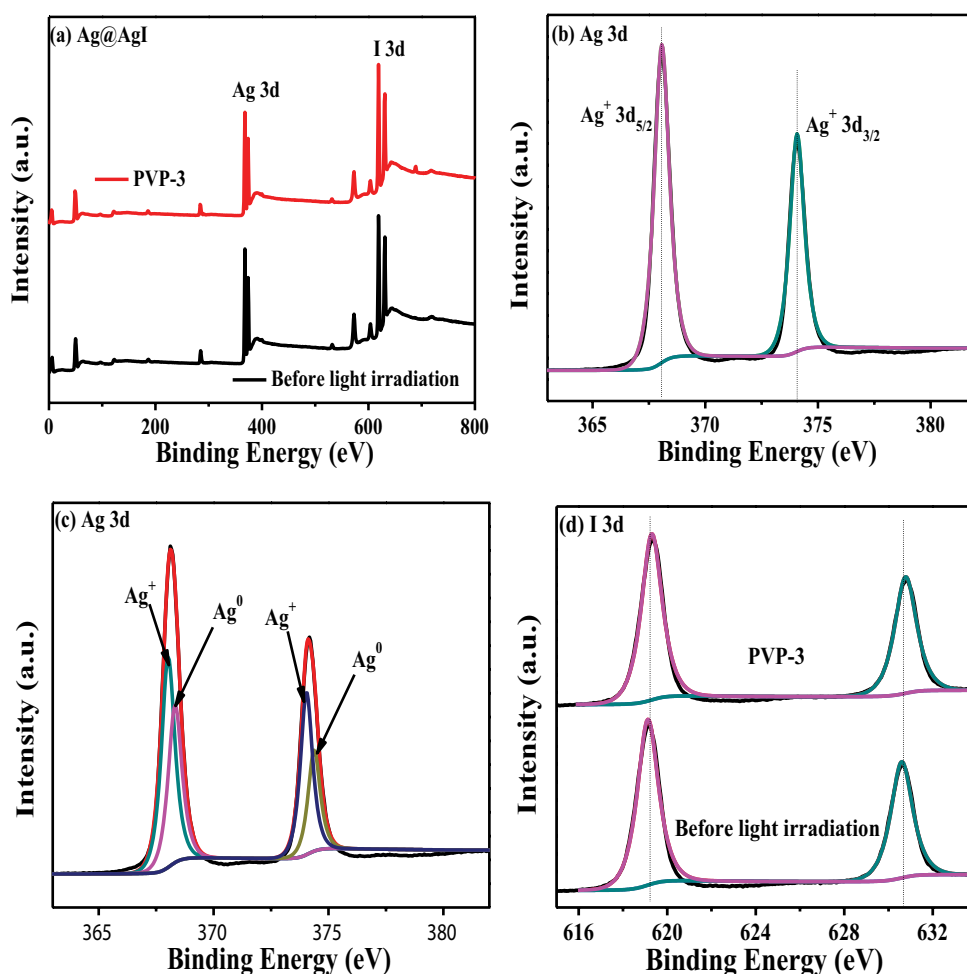
Fig. 3. (a) XPS survey spectrum and (b–d) high-resolution XPS spectra of AgI and Ag@AgI: (b) Ag 3d of AgI, (c) Ag 3d of Ag@AgI, and (d) I 3d of AgI and Ag@AgI.
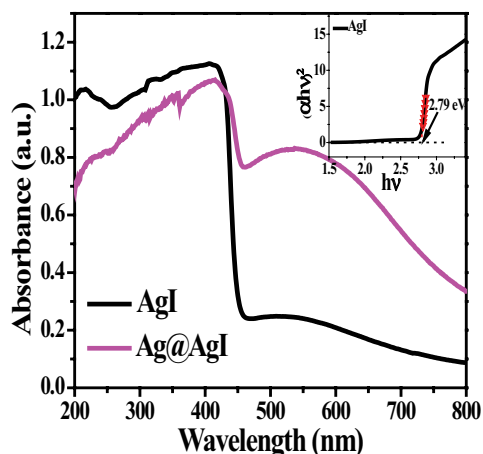
Fig. 4. UV-vis diffuse reflectance spectrum of PVP-3. The inset displays the band gap values estimated from the plotted curves of $(\alpha h\nu)^2$ versus $h\nu$.

visible-light-driven photocatalytic performance. In addition, the optical band gaps (E_g) of the AgI was calculated based on the formula: $(\alpha h\nu)^r = k (h\nu - E_g)$, where α, h, and ν are the absorption coefficient, Planck constant, and light frequency, respectively, k is a constant relative to the material and $r = 2$ as a direct transition semiconductor for AgI [45]. The E_g value is obtained to be 2.79 eV for pure AgI, which is well consistent with previous reports [46].

3.2. Photocatalytic properties

RhB was chosen as the model contaminant to evaluate the photocatalytic activity of the as-prepared samples under visible-light irradiation. Prior to irradiation, the reaction mixture was stirred in the dark for 60 min to achieve an adsorption–desorption equilibrium between the contaminant and photocatalyst. As shown in Fig. 5(a), after 8 min visible-light irradiation, the degradation efficiencies of RhB over PVP-0, PVP-0.5, PVP-1, PVP-3, and PVP-5 photocatalysts are 13.46%, 53.87%, 80.66%, 93.69%, and 90.67%, respectively. The results show that the photocatalytic performance of as-synthesized Ag@AgI has been significantly improved after the amount adjustment of PVP. The composite of PVP-3 shows the highest photocatalytic activity. As shown in Fig. 5(b), the photocatalytic reaction rate can be described by the pseudo-first-order kinetic: $-\ln(C/C_0) = kt$, where t (min) is the irradiation time and k (min^{-1}) is the apparent reaction rate constant. The effect of PVP on the photocatalytic activity of the composites is also directly reflected by the apparent rate constants in Fig. 5(c). It can be seen that for the degradation of RhB, PVP-3 possesses the highest rate constant (0.3446 min^{-1}), which is about 18.9 times than that of PVP-0 (0.0182 min^{-1}). As aforementioned, the addition of PVP favors the preparation of AgI particles with smaller diameter which possesses larger specific surface area and much more active sites. As a result, the photocatalytic activities of the Ag@AgI plasmonic photocatalysts are significantly enhanced. However, when the PVP amount was increased to 5 mmol, the derived Ag@AgI photocatalyst (PVP-5) shows almost the same catalytic activity as PVP-3. This is consistent with the fact that suitable increasing of PVP

favors the formation of smaller and more uniform Ag@AgI nanoparticles. However, when the amount of PVP is beyond 3 mmol, the size of the Ag@AgI nanoparticles shows no further decrease. In addition to the visible-light photocatalytic activity, the recyclability of photocatalysts is another important criterion to evaluate its photocatalytic performance and has a significant effect on its practical application [47]. The stability of the Ag@AgI plasmonic photocatalyst was investigated through the degradation of RhB under the same condition for three successive cycles and the results are shown in Fig. 5(d). The degradation ratios of RhB after being irradiated for 8 min in the three cycles are 93.69%, 91.14%, and 91.13%, respectively, indicating that the photocatalytic activity of the Ag@AgI plasmonic photocatalyst (PVP-3) only slightly decreased after three cycles (from 93.69% to 91.13%). This result proves the high photocatalytic stability of the Ag@AgI composite catalysts. Moreover, the blue-shift of the peak position with time indicates the formation of a series of de-ethylated intermediates (Fig. 5(e)). The similar phenomenon has also been reported in other references and in our previously investigated Bi$_2$WO$_6$-Fe$_3$O$_4$/RhB system [48]. However, in this work, the position of absorption peak only slightly blue-shifted over time, which may be because RhB molecules mainly underwent the cracking of benzene ring rather than de-ethylation during the degradation process [49]. It was found that the color of the RhB solution almost disappeared after 8 min irradiation, indicating the high photocatalytic activity of the Ag@AgI plasmonic photocatalyst.

Furthermore, the degradation products of RhB were identified by GC/MS. The six debenzolized intermediate products were determined as 1-methyl-2-ethyl-benzene, 1,3,5-trimethyl-benzene, phthalic acid 1-isopropyl ester-2-propyl ester, 2-isopropyl-5-methyl-phenol, 2-hydroxy-5-methyl-acetophenone, and phthalic mono (2-ethyl-hexyl) ester. In addition to the intermediates discussed above, some small organic molecules such as 2-oxo-4-methyl-pentanoic acid, succinic acid, 1,4-butanediol, 2-oxo-3-methyl-butyric acid, and 2-hydroxy-propanoic acid were also detected by GC/MS (Table 1). Based on the above experimental results and previous reports [48–50], we proposed the possible photocatalytic degradation pathways of RhB under visible-light irradiation (Fig. 6). Under visible-light irradiation, two pathways simultaneously occur: the de-ethylation process and the cracking of benzene ring [51]. On the one hand, RhB degrades from N, N, N', N'-tetraethylated rhodamine to rhodamine through a series of de-ethylation processes [49,50]. On the other hand, smaller organic molecules were formed during the degradation of the conjugated xanthene structures of both RhB and the de-ethylated intermediates in the decolorization process.

We assume that the concentration of RhB is proportional to the intensity of the absorption peak at 553 nm, and approximately regard the change in absorbance (A/A_0) of RhB as the change in its concentration (C/C_0). A represents the absorbance at 553 nm and A_0 is the initial absorbance of RhB at 553 nm before photodegradation. Fig. 7 shows the curves of C/C_0 versus time (t) during the photocatalytic reaction. As shown, the blank test without any catalyst reveals that the self-photolysis of RhB is negligible. Moreover, it can be seen that by using PVP-3 catalyst, the degradation ratio of RhB reaches 93.69% after 8 min of visible-light irradiation, while the degradation ratio of RhB is only about 19.36% after
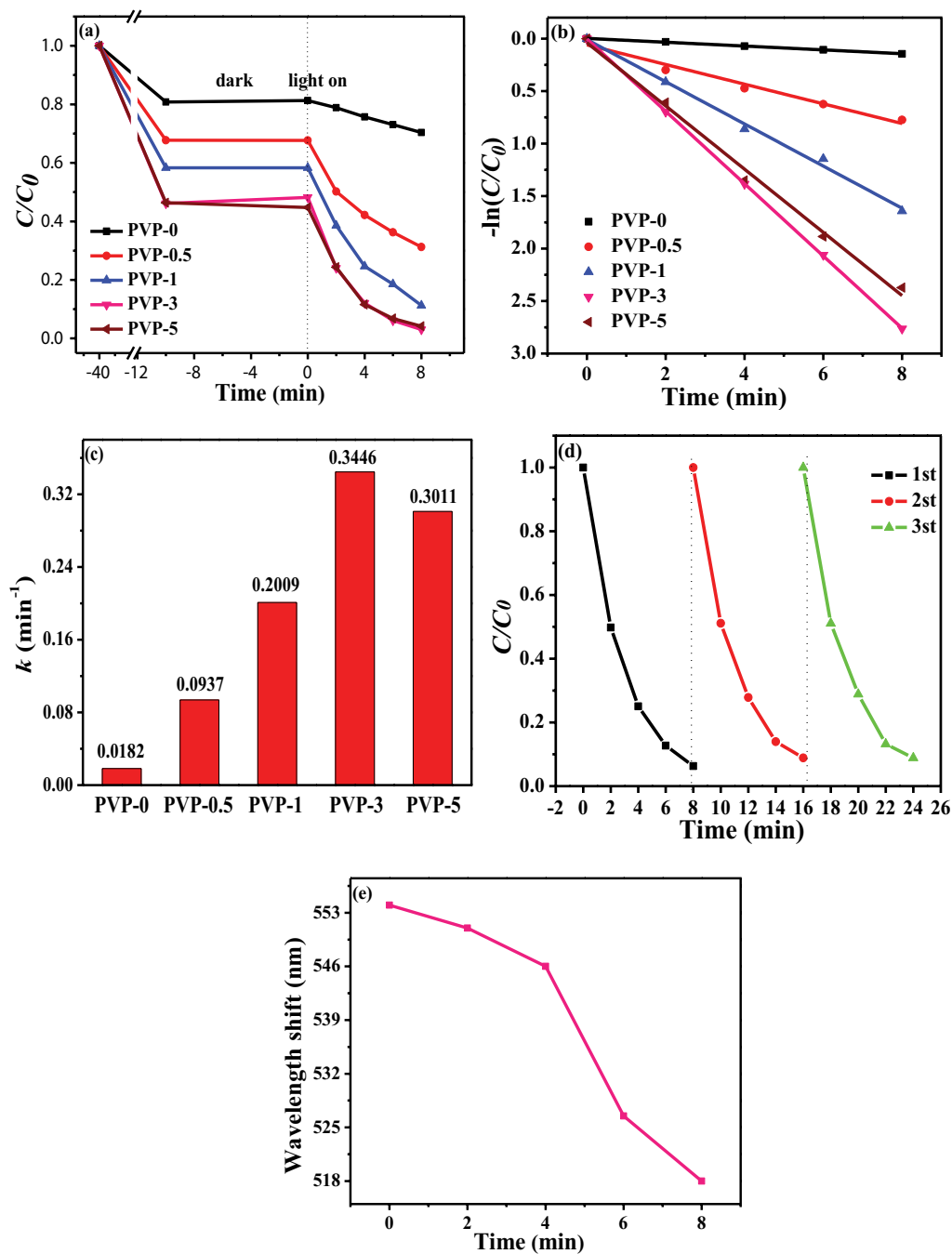
Fig. 5. (a) The photocatalytic degradation of RhB based on the as-prepared samples; (b) pseudo-first-order kinetic curves of the photocatalytic degradation of RhB over different photocatalysts; (c) the rate constants of the photodegradation of RhB with different photocatalysts; (d) cycling runs of the Ag@AgI photocatalyst (PVP-3) in the degradation of RhB under visible-light irradiation; and (e) wavelength shift of the absorption peaks as a function of the photocatalytic time.

12 min irradiation with P25 catalyst (a commercial TiO$_2$ as a benchmark photocatalyst [18]). As a result, the photocatalytic activity of Ag@AgI nanocomposite is much higher than that of P25. The rate constants of the catalysts P25 and Ag@AgI were 0.0172 and 0.3446 min^{-1}, respectively, suggesting that the photocatalytic activity of the as-prepared Ag@AgI photocatalyst is almost 19 times higher than that of the commercial P25.

The interfacial charge transfer and recombination rates of the as-prepared photocatalysts were studied by the photoelectrochemical analysis. Fig. 8 shows the transient photocurrent responses of Ag@AgI photocatalysts under intermittent visible-light irradiation for five on–off cycles. Obviously, with the assistance of PVP, the charge carrier densities of the composites are significantly enhanced. The PVP-3 presents the highest photocurrent response (4.83 µA cm^{-2}), which is about

Table 1
Identification of the degradation products of RhB by GC/MS

m/z	Retention time	Identified intermediates	Structural formula
130.06	3.236	2-Oxo-4-methyl-pentanoic acid	
118.03	3.322	Succinic acid	
120.09	4.060	Benzene, 1-methyl-2-ethyl-	
90.07	4.105	Butane-1,4-diol	
116.05	4.160	2-Oxo-3-methyl-butyric acid	
120.09	4.277	Benzene, 1,3,5-trimethyl-	
90.03	5.513	2-Hydroxy-propionic acid	
250.12	21.403	Phthalic acid 1-isopropyl ester 2-propyl ester	
150.10	26.936	2-Isopropyl-5-methyl-phenol	
150.07	27.440	2-Hydroxy-5-methyl-acetophenone	
278.15	31.245	1,2-Benzenedicarboxylic acid, mono(2-ethylhexyl) ester	
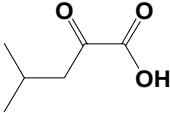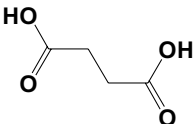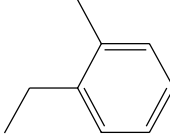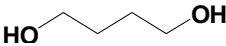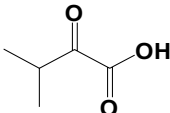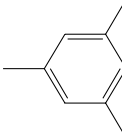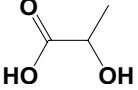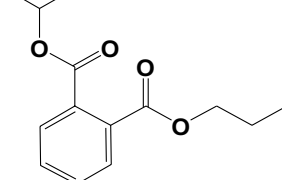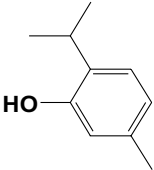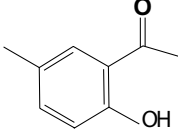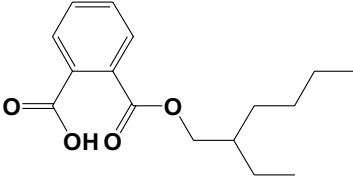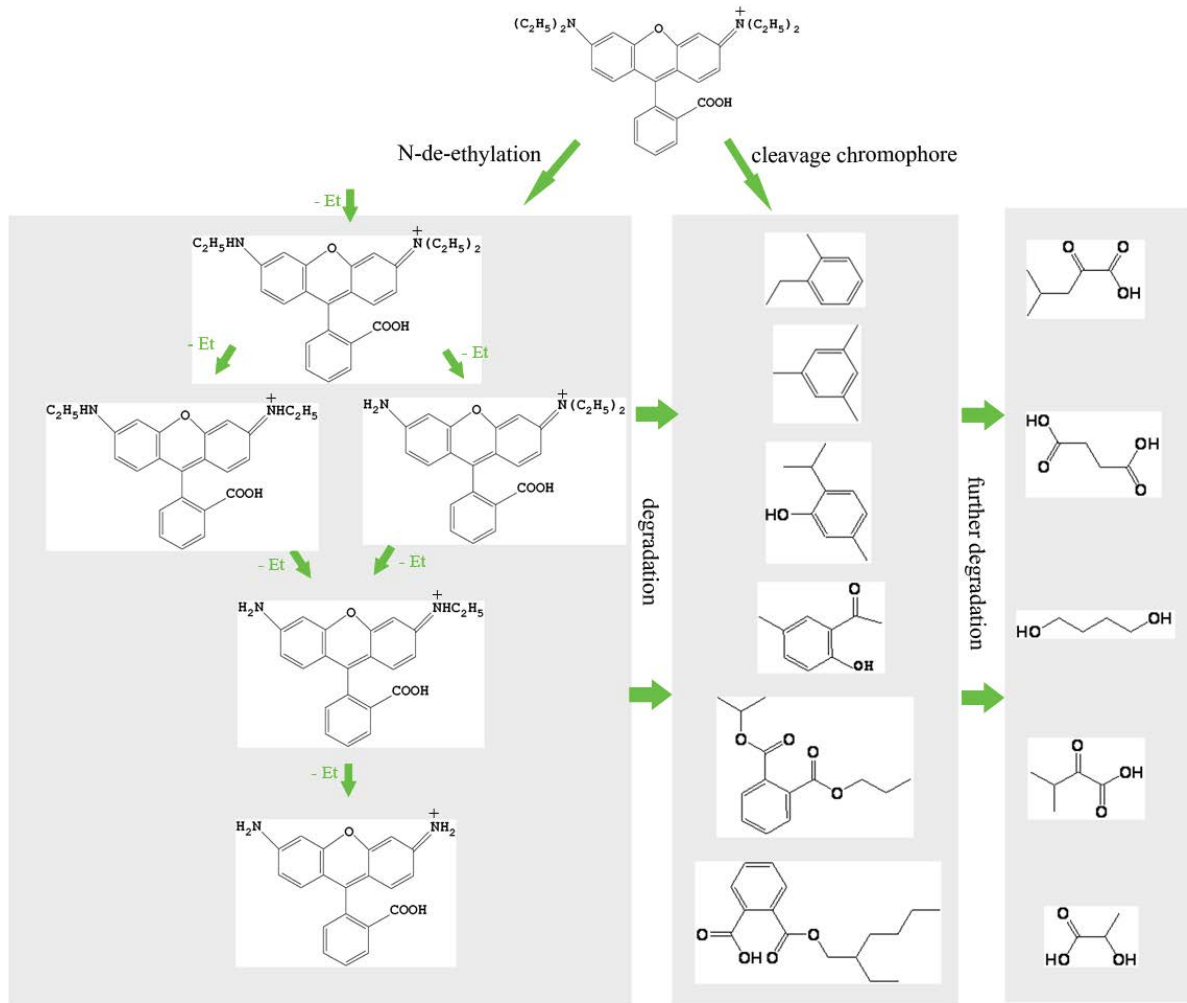
Fig. 6. Proposed degradation pathways for photocatalytic degradation of RhB with Ag@AgI plasmonic photocatalyst.
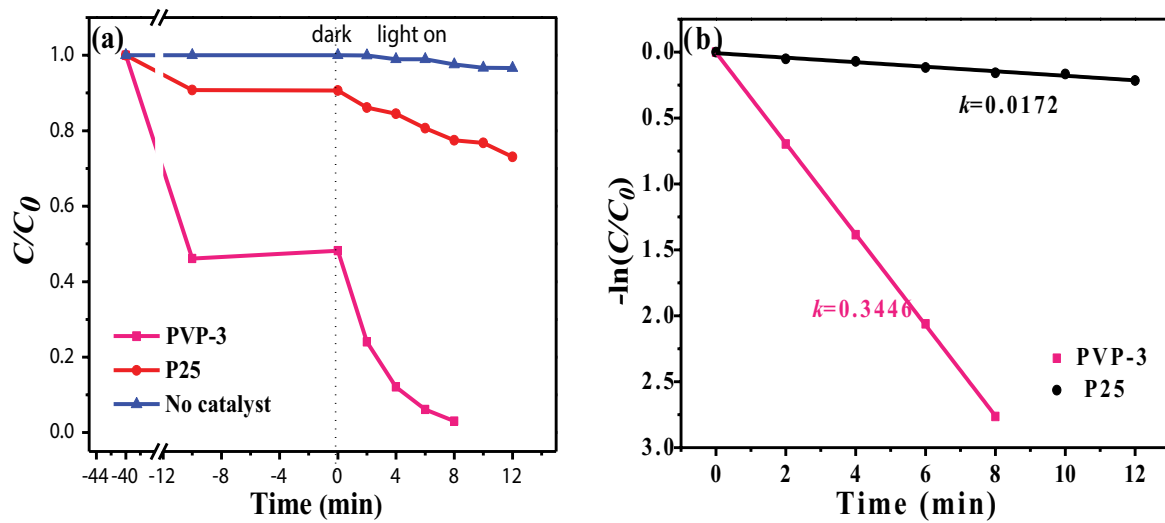
Fig. 7. (a) The photocatalytic degradation efficiencies and (b) first-order plots for the photocatalytic degradation of RhB over Ag@AgI and P25.
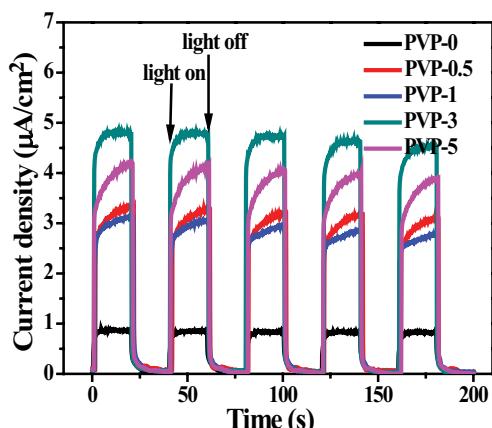
Fig. 8. Transient photocurrent response curves of Ag@AgI photocatalysts.

5.4 times of PVP-0 (0.89 µA cm⁻²). The result indicates that the PVP-3 possesses the highest separation efficiency for the photoinduced charge carriers among these photocatalysts.

It is known that $\cdot O_2^-$, h$^+$ and $\cdot OH$ are three main active species in photocatalytic process. To clarify the dominant active species in the photocatalytic reactions, the trapping experiments were carried out. Benzoquinone (BZQ), disodium ethylenediaminetetraacetate (Na$_2$-EDTA), and isopropanol (IPA) were employed to act as $\cdot O_2^-$, h$^+$, and $\cdot OH$ scavengers, respectively. Fig. 9(a) shows the photodegradation of RhB with PVP-3 photocatalyst after adding various trapping scavengers. The effect of scavengers on the photocatalytic activity of the composite is also directly reflected by the apparent rate constants in Fig. 9(b). The rate constant of PVP-3 without any scavenger is 0.3446 min⁻¹, while the rate constants change into 0.1049, 0.1432, and 0.0062 min⁻¹ when introducing the scavengers of IPA, Na$_2$-EDTA, and BZQ, respectively, indicating that the introduction of IPA and Na$_2$-EDTA into the reaction system could affect the photodegradation efficiency in some degree, while the introduction of BZQ almost completely inhibited the RhB degradation. These results mean that $\cdot O_2^-$ is the main reactive species and h$^+$ and $\cdot OH$ also play some role during the photocatalytic process.

In order to further clarify the photocatalytic mechanism, the ESR measurements of the AgI and PVP-3 were carried out. As shown in Fig. 10(a), no signal of DMPO-$\cdot OH$ was detected in the dark. When exposed to visible-light irradiation, the ESR signal of DMPO-$\cdot OH$ could be observed over AgI and PVP-3
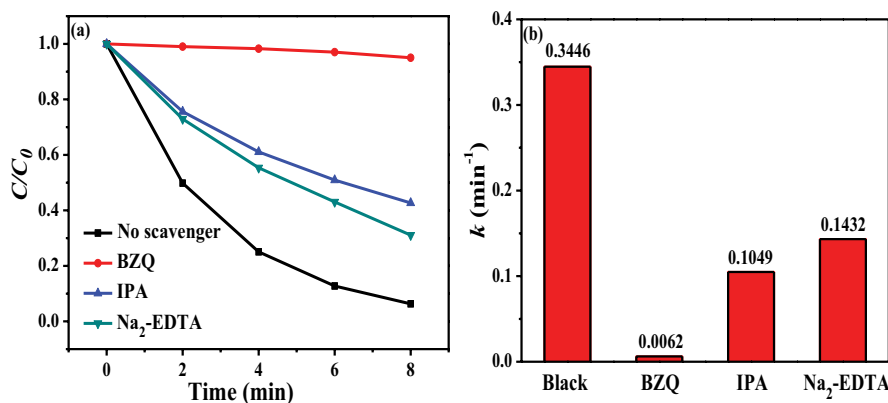
Fig. 9. (a) The trapping experiments of the active species for the photocatalytic reactions based on Ag@AgI photocatalysts and (b) the corresponding rate constants.
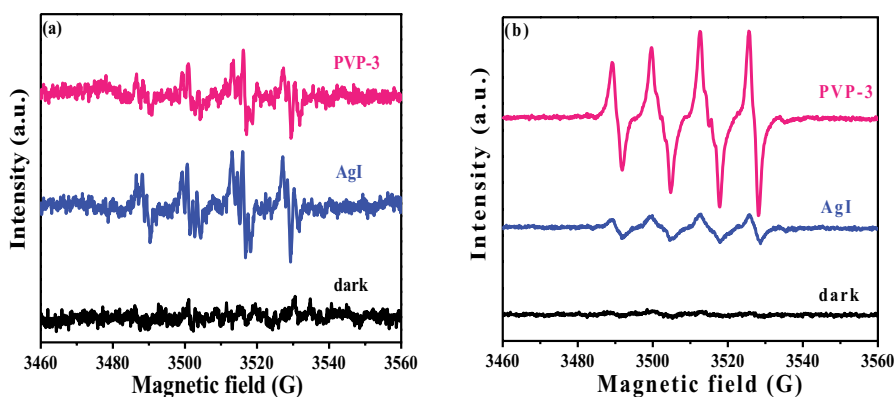
Fig. 10. ESR spectra of (a) DMPO-$\cdot OH$ adducts in aqueous solution and (b) DMPO-$\cdot O_2^-$ adducts in methanol solution recorded with AgI and PVP-3 under visible-light irradiation.

with almost the same intensity, confirming that •OH species plays some role in the photocatalytic processes of these catalysts. As shown in Fig. 10(b), no signal of DMPO-•O_2^- was found in the dark in the presence of PVP-3, proving that no •O_2^- radicals were generated in this condition. In contrast, the four characteristic peaks of the DMPO-•O_2^- adducts were observed over AgI and PVP-3 under visible-light irradiation. Moreover, the DMPO-•O_2^- peaks over PVP-3 are much stronger than those over AgI, indicating that more •O_2^- radicals were generated over PVP-3 than AgI. As PVP-3 has smaller particle sizes and larger specific surface area, it has more reaction sites and therefore produces more •O_2^- radicals. These results are well consistent with those of the trapping experiments.

In order to understand the reason for the excellent photocatalytic performance of the as-prepared Ag@AgI photocatalysts, the photocatalytic mechanism is proposed in Fig. 11 and discussed as follows. It has been reported that the conduction band of AgI is −0.50 eV [42]. According to the formula $E_{CB} = E_{VB} - E_{g'}$ the valence band value of AgI is calculated to
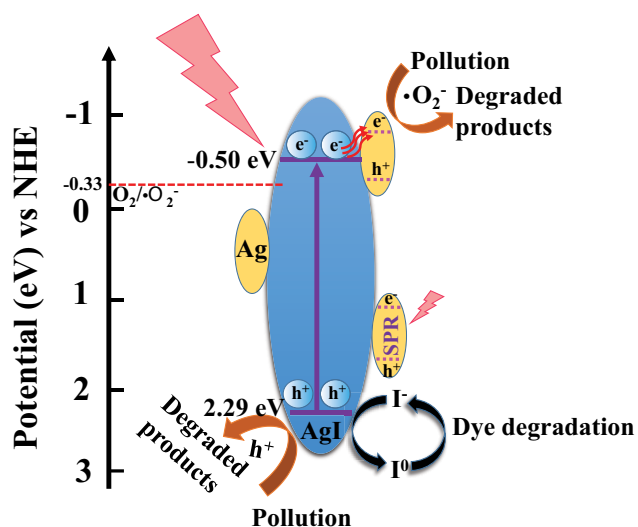
be 2.29 eV. First, since Ag has a strong absorption in the visible region due to its surface plasmonic effect, a large amount of photogenerated electrons and holes could be produced in Ag@AgI nanocomposites [38,52]. Then, due to the synergy effect between the high conductivity of Ag nanoparticles and the polarization field provided by the AgI nanoparticles, the photogenerated electrons could quickly transfer to the surface of Ag nanoparticles, and thus leading to the more efficient separation of the hole–electron pairs. The excited electrons on the surface of Ag are then trapped by the oxygen molecules (O_2) in the solution to form superoxide ions ($O_2^{•-}$) and other reactive species [53]. At the same time, photogenerated holes could not only oxidize the RhB molecules directly, but could be also transferred to iodine ions to oxidize them into iodine atoms at the surface sites of AgI, which could also oxidize RhB dye and reduce themselves to stable iodine ions [54]. The uniform and small size of the as-prepared Ag@AgI nanoparticles could provide large surface area and more reactive sites for the degradation of RhB molecules. In addition, since Ag is generated in situ at the AgI surface, the better interfacial contact between them favors the rapid electron transfer process, which further promotes the separation of the electron–hole pairs [55]. As a result, the as-synthesized Ag@AgI plasmonic photocatalysts could exhibit high photocatalytic activity and cyclic stability. The comparison about the Ag/AgI systems that has been reported in recent years is listed in Table 2.

4. Conclusion

In summary, we have successfully synthesized Ag@AgI nanoparticles by a simple surfactant-assisted precipitation method. The size of Ag@AgI nanoparticles can be well controlled by adjusting the feeding amount of PVP in the reaction solution. The Ag@AgI composites exhibit a significantly enhanced photocatalytic activity in the degradation of RhB molecules under visible-light irradiation compared with P25. Its high photocatalytic activity could be mainly ascribed to the surface plasmonic effect of the Ag metal, uniform and small sizes of the Ag@AgI nanoparticles, and the good contact between Ag and AgI. In addition, the possible pathway and mechanism for the degradation of RhB molecules were also proposed. With high photocatalytic activity and good

Fig. 11. The proposed mechanism for Ag@AgI photocatalysts under visible-light irradiation.

Table 2
A comparison between the Ag@AgI photocatalyst and some related photocatalysts reported previously

Photocatalysts	Pollutants	Light source	Photodegradation rate constant (k)	Reference
Ag/AgI/BiOI	RhB (10 mg L^{-1})	500 W Xe lamp ($\lambda > 420$ nm)	0.8673 h^{-1}	[41]
AgI/Ag/I-(BiO)$_2$CO$_3$	RhB (10 mg L^{-1})	500 W Xe lamp ($\lambda > 420$ nm)	0.62 h^{-1}	[42]
Ag-AgI/Fe$_3$O$_4$@SiO$_2$	RhB (25 mg L^{-1})	250 W metal halide lamp ($\lambda > 420$ nm)	4.98 h^{-1}	[54]
K$_4$Nb$_6$O$_{17}$/Ag@AgI	RhB (10 mg L^{-1})	250 W metal halide lamp ($\lambda > 400$ nm)	(Degradation rates: 83.00% after 40 min irradiation)	[56]
Ag/AgI	RhB (10 mg L^{-1})	250 W metal halide lamp ($\lambda > 400$ nm)	9.60 h^{-1}	[57]
Ag@AgI-modified N, F co-doped TiO$_2$	MO (20 mg L^{-1})	500 W Xe lamp ($\lambda > 400$ nm)	Degradation rates: 95.50% after 90 min irradiation	[58]
α-Fe$_2$O$_3$/Ag/AgX (X = Cl, Br, I)	RhB (10 mg L^{-1})	A mercury lamp (300 W)	0.78 h^{-1}	[59]
Ag@AgI	RhB (10 mg L^{-1})	250 W Xe lamp ($\lambda > 420$ nm)	20.67 h^{-1}	This work

cyclic stability under visible-light irradiation, the Ag@AgI plasmonic photocatalysts may promise potential applications in the degradation of organic pollutants and environmental purification.

References

[1] A. Kudo, Y. Miseki, Heterogeneous photocatalyst materials for water splitting, Chem. Soc. Rev., 38 (2009) 253–278.

[2] U.G. Akpan, B.H. Hameed, Parameters affecting the photo-catalytic degradation of dyes using TiO_2-based photocatalysts: a review, J. Hazard. Mater., 170 (2009) 520–529.

[3] H.G. Yang, C.H. Sun, S.Z. Qiao, J. Zou, G. Liu, S.C. Smith, H.M. Cheng, G.Q. Lu, Anatase TiO_2 single crystals with a large percentage of reactive facets, Nature, 453 (2008) 638–641.

[4] X. Zhang, F. Zhang, K.Y. Chan, Synthesis of titania-silica mixed oxide mesoporous materials, characterization and photocatalytic properties, Appl. Catal., A, 284 (2005) 193–198.

[5] X.B. Chen, S.S. Mao, Titanium dioxide nanomaterials: synthesis, properties, modifications, and applications, Chem. Rev., 107 (2007) 2891–2959.

[6] R. Sasikala, A.R. Shirole, V. Sudarsan, V.S. Kamble, C. Sudakar, R. Naik, R. Rao, S.R. Bharadwaj, Role of support on the photocatalytic activity of titanium oxide, Appl. Catal., A, 390 (2010) 245–252.

[7] H.X. Li, Z.F. Bian, J. Zhu, Y.N. Huo, H. Li, Y.F. Lu, Mesoporous Au/TiO_2 nanocomposites with enhanced photocatalytic activity, J. Am. Chem. Soc., 129 (2007) 4538–4539.

[8] J.C. Yu, L.Z. Zhang, Z. Zheng, J.C. Zhao, Synthesis and characterization of phosphated mesoporous titanium dioxide with high photocatalytic activity, Chem. Mater., 15 (2003) 2280–2286.

[9] Y.J. Lin, S. Zhou, X.H. Liu, S. Sheehan, D.W. Wang, $TiO_2/TiSi_2$ heterostructures for high-efficiency photoelectrochemical H_2O splitting, J. Am. Chem. Soc., 131 (2009) 2772–2773.

[10] S.U.M. Khan, M. Al-Shahry, W.B. Ingler, Efficient photochemical water splitting by a chemically modified n-TiO_2, Science, 297 (2002) 2243–2245.

[11] R. Asahi, T. Morikawa, T. Ohwaki, K. Aoki, Y. Taga, Visible-light photocatalysis in nitrogen-doped titanium oxides, Science, 293 (2001) 269–271.

[12] T. Ohno, T. Mitsui, M. Matsumura, Photocatalytic activity of S-doped TiO_2 photocatalyst under visible light, Chem. Lett., 32 (2003) 364–365.

[13] P. Dhiman, M. Naushad, K.M. Batoo, A. Kumar, G. Sharma, A.A. Ghfar, G. Kumar, M. Singh, Nano $Fe_xZn_{1-x}O$ as a tuneable and efficient photocatalyst for solar powered degradation of bisphenol A from aqueous environment, J. Cleaner Prod., 165 (2017) 1542–1556.

[14] M.I. Litter, Heterogeneous photocatalysis: transition metal ions in photocatalytic systems, Appl. Catal., B, 23 (1999) 89–114.

[15] L.M. Peter, D.J. Riley, E.J. Tull, K.G.U. Wijayantha, Photo-sensitization of nanocrystalline TiO_2 by self-assembled layers of CdS quantum dots, Chem. Commun., 10 (2002) 1030–1031.

[16] C.C. Chen, W.H. Ma, J.C. Zhao, Semiconductor-mediated photodegradation of pollutants under visible-light irradiation, Chem. Soc. Rev., 39 (2010) 4206–4219.

[17] A. Kumar, A. Kumar, G. Sharma, M. Naushad, F.J. Stadler, A.A. Ghfar, P. Dhiman, R.V. Saini, Sustainable nano-hybrids of magnetic biochar supported g-$C_3N_4/FeVO_4$ for solar powered degradation of noxious pollutants-Synergism of adsorption,

[18] photocatalysis & photo-ozonation, J. Cleaner Prod., 165 (2017) 431–451.

[18] A. Kumar, Shalini, G. Sharma, M. Naushad, A. Kumar, S. Kalia, C. Guo, G.T. Mola, Facile hetero-assembly of superparamagnetic $Fe_3O_4/BiVO_4$ stacked on biochar for solar photo-degradation of methyl paraben and pesticide removal from soil, J. Photochem. Photobiol., A, 337 (2017) 118–131.

[19] K. Awazu, M. Fujimaki, C. Rockstuhl, J. Tominaga, H. Murakami, Y. Ohki, N. Yoshida, T. Watanabe, A plasmonic photocatalyst consisting of silver nanoparticles embedded in titanium dioxide, J. Am. Chem. Soc., 130 (2008) 1676–1680.

[20] S. Link, M.A. El-Sayed, Spectral properties and relaxation dynamics of surface plasmon electronic oscillations in gold and silver nanodots and nanorods, J. Phys. Chem. B, 103 (1999) 8410–8426.

[21] T.K. Sau, A.L. Rogach, F. Jackel, T.A. Klar, J. Feldmann, Properties and applications of colloidal nonspherical noble metal nanoparticles, Adv. Mater., 22 (2010) 1805–1825.

[22] X. Chen, H.Y. Zhu, J.C. Zhao, Z.F. Zheng, X.P. Gao, Visible-light-driven oxidation of organic contaminants in air with gold nanoparticle catalysts on oxide supports, Angew. Chem. Int. Ed., 47 (2008) 5353–5356.

[23] Q. Xiang, J. Yu, B. Cheng, H.C. Ong, Microwave-hydrothermal preparation and visible-light photoactivity of plasmonic photocatalyst Ag-TiO_2 nanocomposite hollow spheres, Chem. Asian J., 5 (2010) 1466–1474.

[24] R. Saravanan, S. Agarwal, V.K. Gupta, M.M. Khan, F. Gracia, E. Mosquera, V. Narayanan, A. Stephen, Line defect Ce^{3+} induced $Ag/CeO_2/ZnO$ nanostructure for visible-light photocatalytic activity, J. Photochem. Photobiol., A, 353 (2018) 499–506.

[25] P. Wang, B.B. Huang, X.Y. Qin, X.Y. Zhang, Y. Dai, J.Y. Wei, M.H. Whangbo, Ag@AgCl: a highly efficient and stable photocatalyst active under visible light, Angew. Chem. Int. Ed., 47 (2008) 7931–7933.

[26] P. Wang, B.B. Huang, X.Y. Zhang, X.Y. Qin, Y. Dai, Z.Y. Wang, Z.Z. Lou, Highly efficient visible light plasmonic photocatalysts Ag@Ag(Cl,Br) and Ag@AgCl-AgI, ChemCatChem, 3 (2011) 360–364.

[27] P. Wang, B.B. Huang, Z.Z. Lou, X.Y. Zhang, X.Y. Qin, Y. Dai, Z.K. Zheng, X.N. Wang, Synthesis of highly efficient Ag@AgCl plasmonic photocatalysts with various structures, Chem. Eur. J., 16 (2010) 538–544.

[28] P. Wang, B.B. Huang, Q.Q. Zhang, X.Y. Zhang, X.Y. Qin, Y. Dai, J. Zhan, J.X. Yu, H.X. Liu, Z.Z. Lou, Highly efficient visible light plasmonic photocatalyst Ag@Ag(Br,I), Chem. Eur. J., 16 (2010) 10042–10047.

[29] M.Y. Kang, X.Y. Zhang, L.W. Liu, Q.W. Zhou, M.L. Jin, G.F. Zhou, X.S. Gao, X.B. Lu, Z. Zhang, J.M. Liu, High-density ordered Ag@Al_2O_3 nanobowl arrays in applications of surface-enhanced Raman spectroscopy, Nanotechnology, 27 (2016) 165304.

[30] C.H. An, S. Peng, Y.G. Sun, Facile synthesis of sunlight-driven AgCl:Ag plasmonic nanophotocatalyst, Adv. Mater., 22 (2010) 2570–2574.

[31] D.Y. Wu, M.C. Long, Realizing visible-light-induced self-cleaning property of cotton through coating N-TiO_2 film and loading AgI particles, ACS Appl. Mater. Interfaces, 3 (2011) 4770–4774.

[32] B. Xue, T. Sun, J.K. Wu, F. Mao, W. Yang, AgI/TiO_2 nanocomposites: ultrasound-assisted preparation, visible-light induced photocatalytic degradation of methyl orange and antibacterial activity, Ultrason. Sonochem., 22 (2015) 1–6.

[33] X.L. Miao, X.P. Shen, J.J. Wu, Z.Y. Ji, J.H. Wang, L.R. Kong, M.M. Liu, C.S. Song, Fabrication of an all solid Z-scheme photocatalyst gC_3N_4/GO/AgBr with enhanced visible light photocatalytic activity, Appl. Catal., A, 539 (2017) 104–113.

[34] D.L. Chen, S.H. Yoo, Q.S. Huang, G. Ali, S.O. Cho, Sonochemical synthesis of Ag/AgCl nanocubes and their efficient visible-light-driven photocatalytic performance, Chem. Eur. J., 18 (2012) 5192–5200.

[35] J. Jiang, H. Li, L.Z. Zhang, New insight into daylight photocatalysis of AgI@Ag: synergistic effect between semiconductor photocatalysis and plasmonic photocatalysis, Chem. Eur. J., 18 (2012) 6360–6369.

[36] J. Jiang, L.Z. Zhang, Rapid microwave-assisted nonaqueous synthesis and growth mechanism of AgCl/Ag, and its daylight-driven plasmonic photocatalysis, Chem. Eur. J., 17 (2011) 3710–3717.

[37] H. Wang, X.F. Lang, J. Gao, W. Liu, D. Wu, Y.M. Wu, L. Guo, J.H. Li, Polyhedral AgI microcrystals with an increased percentage of exposed {111} facets as a highly efficient visible-light photocatalyst, Chem. Eur. J., 18 (2012) 4620–4626.

[38] Z.C. Wang, J.H. Liu, W. Chen, Plasmonic Ag/AgI nanohybrid: synergistic effect of SPR with photographic sensitivity for enhanced photocatalytic activity and stability, Dalton Trans., 41 (2012) 4866–4870.

[39] Q.L. Huang, S.P. Wen, X.S. Zhu, Synthesis and characterization of an AgI/Ag hybrid nanocomposite with surface-enhanced Raman scattering performance and photocatalytic activity, RSC Adv., 4 (2014) 37187–37192.

[40] S. Feng, H. Xu, L. Liu, Y.H. Song, H.M. Li, Y.G. Xu, J.X. Xia, S. Yin, Y. Yan, Controllable synthesis of hexagon-shaped β-AgI nanoplates in reactable ionic liquid and their photocatalytic activity, Colloids Surf., A, 410 (2012) 23–30.

[41] H.L. Lin, Y.J. Zhao, Y.J. Wang, J. Cao, S.F. Chen, Controllable in-situ synthesis of Ag/BiOI and Ag/AgI/BiOI composites with adjustable visible light photocatalytic performances, Mater. Lett., 132 (2014) 141–144.

[42] L. Liang, J. Cao, H.L. Lin, M.Y. Zhang, X.M. Guo, S.F. Chen, A novel double visible light active Z-scheme AgI/Ag/I-(BiO)₂CO₃ composite: automatic formation of Ag bridge in the photocatalytic process, Mater. Res. Bull., 94 (2017) 291–297.

[43] D.D. Yu, J. Bai, H.O. Liang, J.Z. Wang, C.P. Li, Fabrication of a novel visible-light-driven photocatalyst Ag-AgI-TiO₂ nanoparticles supported on carbon nanofibers, Appl. Surf. Sci., 349 (2015) 241–250.

[44] Y.P. Bi, S.X. Ouyang, J.Y. Cao, J.H. Ye, Facile synthesis of rhombic dodecahedral AgX/Ag₃PO₄ (X = Cl, Br, I) heterocrystals with enhanced photocatalytic properties and stabilities, Phys. Chem. Chem. Phys., 13 (2011) 10071–10075.

[45] H.F. Cheng, B.B. Huang, Y. Dai, X.Y. Qin, X.Y. Zhang, One-step synthesis of the nanostructured AgI/BiOI composites with highly enhanced visible-light photocatalytic performances, Langmuir, 26 (2010) 6618–6624.

[46] Z.B. Xiang, Y. Wang, P. Ju, Y. Long, D. Zhang, Facile fabrication of AgI/BiVO₄ composites with enhanced visible photocatalytic degradation and antibacterial ability, J. Alloys Compd., 721 (2017) 622–627.

[47] S.K. Li, F.Z. Huang, Y. Wang, Y.H. Shen, L.G. Qiu, A.J. Xie, S.J. Xu, Magnetic Fe₃O₄@C@Cu₂O composites with bean-like core/shell nanostructures: synthesis, properties and application in recyclable photocatalytic degradation of dye pollutants, J. Mater. Chem., 21 (2011) 7459–7466.

[48] X. Xu, X.P. Shen, G.X. Zhu, L.Q. Jing, X.S. Liu, K.M. Chen, Magnetically recoverable Bi₂WO₆-Fe₃O₄ composite photocatalysts: fabrication and photocatalytic activity, Chem. Eng. J., 200–202 (2012) 521–531.

[49] K. Yu, S.G. Yang, H. He, C. Sun, C.G. Gu, Y.M. Ju, Visible light-driven photocatalytic degradation of rhodamine B over NaBiO₃: pathways and mechanism, J. Phys. Chem. A, 113 (2009) 10024–10032.

[50] Z. He, C. Sun, S.G. Yang, Y.C. Ding, H. He, Z.L. Wang, Photocatalytic degradation of rhodamine B by Bi₂WO₆ with electron accepting agent under microwave irradiation: mechanism and pathway, J. Hazard. Mater., 162 (2009) 1477–1486.

[51] C.C. Chen, X.Z. Li, W.H. Ma, J.C. Zhao, H. Hidaka, N. Serpone, Effect of transition metal ions on the TiO₂-assisted photodegradation of dyes under visible irradiation: a probe for the interfacial electron transfer process and reaction mechanism, J. Phys. Chem. B, 106 (2002) 318–324.

[52] M.R. Hoffmann, S.T. Martin, W. Choi, D.W. Bahnemann, Environmental applications of semiconductor photocatalysis, Chem. Rev., 95 (1995) 69–96.

[53] S.S. Soni, M.J. Henderson, J.F. Bardeau, A. Gibaud, Visible-light photocatalysis in titania-based mesoporous thin films, Adv. Mater., 20 (2008) 1493–1498.

[54] J.F. Guo, B. Ma, A. Yin, K.N. Fan, W.L. Dai, Photodegradation of rhodamine B and 4-chlorophenol using plasmonic photocatalyst of Ag-AgI/Fe₃O₄@SiO₂ magnetic nanoparticle under visible light irradiation, Appl. Catal., B, 101 (2011) 580–586.

[55] L. Han, P. Wang, C.Z. Zhu, Y.M. Zhai, S.J. Dong, Facile solvothermal synthesis of cube-like Ag@AgCl: a highly efficient visible light photocatalyst, Nanoscale, 3 (2011) 2931–2935.

[56] W.Q. Cui, H. Wang, Y.H. Liang, L. Liu, B.X. Han, Preparation of Ag@AgI-intercalated K₄Nb₆O₁₇ composite and enhanced photocatalytic degradation of Rhodamine B under visible light, Catal. Commun., 36 (2013) 71–74.

[57] Y. Liang, H. Wang, L. Liu, P. Wu, W. Cui, J.G. McEvoy, Z. Zhang, Microwave-assisted synthesis of a superfine Ag/AgI photocatalyst with high activity and excellent durability, J. Mater. Sci., 50 (2015) 6935–6946.

[58] Z. Zhao, L. Zhu, J. Fan, Ag@AgX (X = Cl, Br, I) modified N,F codoped TiO₂ nanotubes as effective photocatalyst, Mater. Technol., 29 (2014) A3–A8.

[59] L.L. Sun, W. Wu, Q.Y. Tian, M. Lei, J. Liu, X.H. Xiao, X.D. Zheng, F. Ren, C.Z. Jiang, In situ oxidation and self-assembly synthesis of dumbbell-like α-Fe₂O₃/Ag/AgX (X = Cl, Br, I) heterostructures with enhanced photocatalytic properties, ACS Sustain. Chem. Eng., 4 (2016) 1521–1530.